X-ray Transparent Proton-Exchange Membrane Fuel Cell Design for In Situ Wide and Small Angle Scattering Tomography

Isaac Martens[a,b], Antonis Vamvakeros[a,c,d], Raphael Chattot[a,e], Maria V. Blanco[a], Miika Rasola[a,f,g], Janne Pusa[a,e,h], Simon D. M. Jacques[c], Dan Bizzotto[b], David P. Wilkinson[i], Bastian Ruffmann[j], Stefan Heidemann[j], Veijo Honkimäki[a], Jakub Drnec[a,*]

[a] *European Synchrotron Radiation Facility, Grenoble, France*
[b] *Advanced Materials and Process Engineering Laboratories, Department of Chemistry, University of British Columbia, Vancouver, Canada*
[c] *Finden Ltd.,Oxfordshire, UK*
[d] *Department of Chemistry, University College London, London, UK*
[e] *Université Grenoble Alpes, LEPMI, Grenoble, France*
[f] *Helsinki Institute of Physics, Helsinki, Finland*
[g] *Department of Physics, University of Helsinki, Finland*
[h] *Department of Applied Physics, Aalto University, Espoo, Finland*
[i] *Department of Chemical Engineering, University of British Columbia, Vancouver, Canada*
[j] *Baltic Fuel Cells, Schwerin, Germany*

Abstract

We have constructed a $5\,cm^2$ proton exchange membrane hydrogen fuel cell optimized for transparency of high energy X-rays. This cell allows for in situ elastic scattering measurements (WAXS, SAXS) during electrochemical operation with minimal trade-offs in cell performance vs benchtop designs, and is capable of reaching automotive current densities. A key feature is that the beam enters the cell at grazing incidence to the electrodes, massively increasing the effective pathlength and therefore the signal-to-background ratio. The 360° transparency in the plane of the sample permits imaging coupled with advanced techniques, such as X-ray diffraction computed tomography.

Keywords: PEMFC, X-ray scattering, tomography, XRD-CT

*Corresponding author
Email address: drnec@esrf.fr (Jakub Drnec)

1. Introduction

The ongoing commercialization of fuel cells and other clean energy technologies increasingly require advances in fundamental understanding of heterogeneous buried interfaces over the life cycle of the device. Hard X-rays are a well-suited tool for probing structural evolution in such complex electrochemical energy systems given their large penetration and small wavelengths allowing characterization across a wide range of length scales. Recent developments in synchrotron hardware have enabled the construction of beamlines with unprecedented flux at high photon energies [1, 2], which allow for more sophisticated sample environments [3]. Here we describe a design of a proton exchange membrane hydrogen fuel cell (PEMFC) with high X-ray transmission used for in situ wide and small angle high energy X-ray scattering (WAXS and SAXS) measurements with no trade-offs in cell performance. Automotive current densities can be stably achieved during measurements, up to several $\mathrm{A\,cm^{-2}}$.

A key advance in the cell and measurement design is the use of in-plane geometry and microfocused beams [4]. Instead of analyzing the layered membrane electrode assembly (MEA) composites through the sample plane, where the effective pathlength is on the order of 10 µm, the X-ray beam is introduced at grazing incidence to the sample plane. This approach allows for pathlengths up to several cm through each material in the composite, which greatly improves the desired signal-to-background ratio. The latter factor is critical for X-ray scattering experiments on complex and multi-component samples, where deconvolution of overlapping signals is a longstanding challenge [5].

Understanding the microscopic spatial and chemical heterogeneities present in electrochemical devices is a critical factor in improving the performance and durability of these systems.[6–9] Hard X-ray diffraction computed tomography (XRD-CT) is an excellent technique for probing these characteristics, non-destructively and under in situ/ operando conditions [10–16]. Because tomographic datasets are typically recorded as a series of cross section images (xy 'slices'), thin films and flat samples can be efficiently mapped in this mea-

surement geometry. The presented X-ray PEMFC is optimised for tomography applications, and offers complete 360° transparency during rotation. This rotational symmetry is critical for reducing reconstruction artefacts, and dramatically improves the quality of the final data. The low background of dark-field scattering vs conventional bright-field absorption tomography simultaneously enhances image contrast, and extends the sample size over which high resolution imaging is possible [17].

The main aim for the development of the presented cell is to gain a better understanding of the complex structure-function relationships and degradation phenomena. Corrosion, dealloying, and ripening of cathode catalyst nanoparticles are leading causes of performance loss over the lifetime of a fuel cell. Investigation of these processes usually involves low throughput imaging (i.e., high resolution electron microscopy) which requires destructive disassembly of the MEA. New, in situ techniques which can repeatedly probe identical locations throughout the lifetime of a device are necessary to understand aging phenomena with increased detail.[18]. Furthermore, the power produced by a PEMFC is frequently limited by water-transport considerations at high current densities and only a few techniques are capable of dynamically imaging hydration at the necessary spatial and temporal resolution.[19, 20] Hard X-ray scattering is well-positioned to probe the chemistry, composition and microstructure at all spatial scales and can give a critical insight into the operational devices.[21]

In this work, we demonstrate how the current capabilities of synchrotron source matched with advanced sample environments offer a powerful platform for investigating these phenomena. We anticipate the advances offered by next generation light sources are likely to improve the spatial and temporal resolution of in situ WAXS/SAXS, as well as the convenience of these measurements.

Previous reports using in situ high energy WAXS on fuel cell samples have suffered from cell design as a result of through-plane or large incidence angle geometry [22–24]. This reduces signal-to-background ratio and makes the data analysis more challenging. From an experimental point of view, this is typically overcome by using electrodes with high catalyst loadings ($>0.5\,\mathrm{mg_{Pt}\,cm^{-2}}$).

However, such cells exhibit decreased interconnection between the catalyst nanoparticles and are less relevant to state-of-the-art, low-loading electrodes. Here we show that our cell geometry places larger quantities of electrocatalyst into the optical path with a much simpler configuration, and is compatible with fuel cell electrodes carrying commercially relevant Pt loadings (0.04-0.4 $mg_{Pt}\,cm^{-2}$). At these trace levels, even sensitive techniques can struggle to obtain good signal-to-noise ratios in through-plane transmission mode [25]. The electrochemical connectivity of thin film catalyst layers is also vastly improved, enabling in situ characterization during cycling experiments [23, 26–28]. The use of grazing incidence geometries to improve surface sensitivity has long been appreciated [29–32], but to the authors' knowledge there are no in-situ PEM fuel cell studies reported using this configuration.

2. Experimental

All X-ray measurements were performed at beamline ID31 at the European Synchrotron Radiation Facility (ESRF). A monochromated beam (E = 78 keV, flux = 10^{13} photons/s) was focused on the sample to the final size of 3 × 20 μm^2 (vertical × horizontal). The cell was mounted in such way that the MEA plane was positioned parallel to the horizontal plane of the beam (Figure 1A). A Pilatus 3X CdTe 2M hybrid photon-counting area detector positioned 504 mm from the cell was used for acquisition of diffraction patterns. Si photodiodes were used to record the flux in Figure 1C.

The 5 cm^2 fuel cell was controlled by a test station (FCS-4M-100W, Lean-Cat Fuel Cell Technologies) to manipulate the anode and cathode voltages, temperatures, gas pressures, gas flow rates, and humidities. A control system was developed to automatically detect membrane puncture events and flush the setup with inert gas, in order to safely analyze samples to the point of failure. Commercial, seven layer conventional PEMFC MEAs were used. The data in Figure 2 were collected using a commercial MEA (Johnson Matthey Fuel Cells) with 0.44/0.04 $mg_{Pt}\,cm^{-2}$ catalyst coating (40wt% Pt on Vulcan XC72) as the

cathode/anode respectively on a 17 µm proprietary ionomer membrane. The data in Figure 3 were collected using a commercial MEA (Bio-Logic Science Instruments) with a symmetrical 0.5 $mg_{Pt}\,cm^{-2}$ catalyst coating on a Nafion 115 membrane. Both samples were hotpressed with gas diffusion media coated with microporous layers (Sigracet 25BC) against each electrode (1 kpsi, 60 s, 120°C). Kapton subgasketing surrounding the active area of the MEA was used to create a leak-free seal with the o-rings on the cell.

2.1. Diffraction tomography

The tomographic measurements were made with 231 translation steps (translation step size of 200 µm, covering 0-180° angular range probing in total 231 angles (i.e. 231 line scans). The translation motor velocity was 1.5 mm/s. The detector calibration was performed using a CeO_2 NIST standard. Every 2D diffraction image was converted to a 1D powder diffraction pattern after applying a light 10% trimmed mean filter to remove any outliers using the pyFAI software [33, 34]. The final XRD-CT images (i.e. reconstructed data volumes) were reconstructed using the filtered back projection algorithm.

3. Results and Discussion

3.1. PEM fuel cell design

The cell body, shown in Figure 1, was machined from polyether ether ketone (PEEK). The cell body itself holds both flowfield plates together, without metallic posts which would obstruct the beampath during cell rotation. A low profile threaded aluminum ring mounts the cell body against the bottom heatsink. This ring partially attenuates the lower part of the 2D diffraction pattern and this needs to be accounted for during the data analysis. An internal thread inside the upper housing allows compression of the two flow fields against the sample with controllable, homogeneously distributed mechanical pressure. The graphite flow fields are attached to brass and copper heat sinks with embedded thermocouples and cartridge heaters. The current is collected on the heat sinks,

while the potential is measured directly on the graphite flowfield. A parallel flow field design was selected such that X-rays can transit the length of the cell without passing through thick layers of graphite. A very small flow field pitch (1 mm) minimizes the mechanical distortion to the PEMFC and keeps the sample flat, improving the quality of the alignment. Precise micro-machining of the graphite plate allows the channel edges to be used as an X-ray knife edge alignment tool. The heatsink baseplate can be directly mounted onto the beamline translation stage, maintaining electrical isolation with ceramic washers. This feature, plus matching pegs in the upper and lower cell body, enable samples to be quickly changed without time-consuming optical realignment. Fluoropolymer o-rings seal the flow fields against the PEM sample, and are compatible with most common subgasket electrode designs.

Anticipating that X-ray spectroscopy at lower X-ray energies may also be of interest, a channel was cut in the cell to provide access for through-plane transmission mode measurements [23, 35–37]. The flow field was thinned in this location, such that the beam path is reduced to 2 mm of graphite, plus the sample thickness. The attenuation of X-rays from the cell at the Pt L-III edge is calculated at 40%, which is sufficient for quantitative spectroscopy. A cone shaped volume was also machined into the bottom heatsink to provide a exit path for through-plane diffraction experiments.

3.2. X-ray characterization

The total attenuation was measured at a variety of X-ray energies in the grazing incidence mode (Figure 1H). The Pt catalyst contributes the majority of the attenuation, and the optical transparency is therefore greatly dependent on the catalyst loading. The transmission was measured both through the plane of the catalyst layer inside the dry, assembled cell, and in the gas channel immediately above the MEA. At modern synchrotron beamlines, photon energy can be freely selected to optimize the sample penetration and range of observed reciprocal space [4, 38]. For a typical MEA with Pt catalyst, a photon energy of 78 keV (below the Pt K-α edge at 78.3 keV) provides a good balance between a

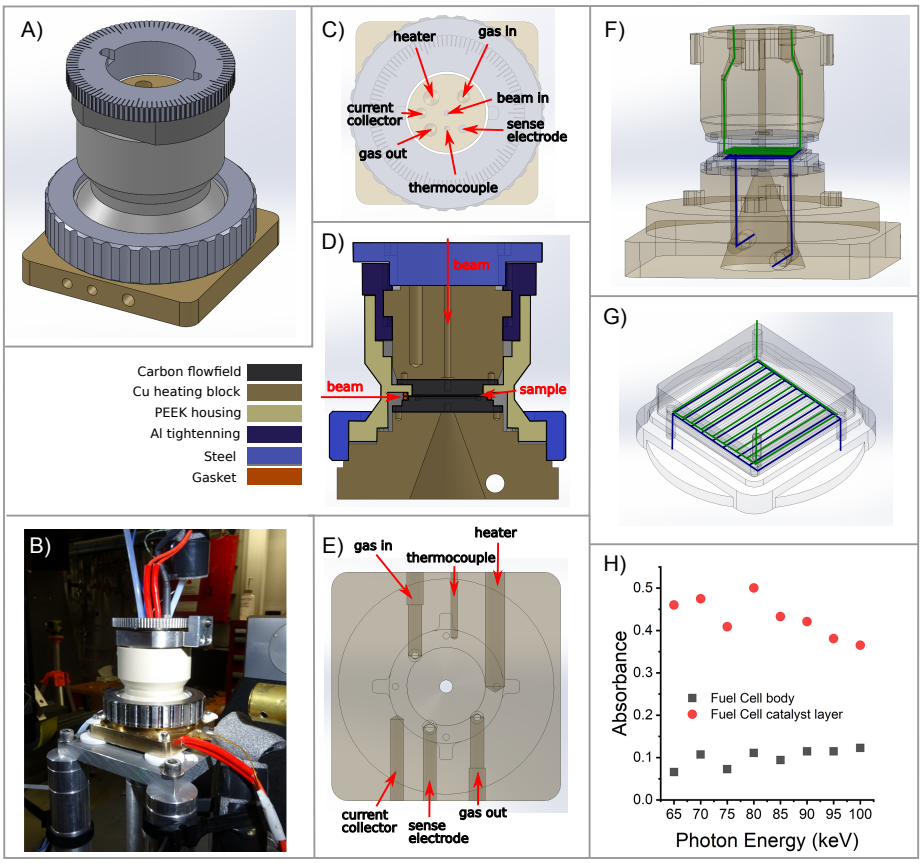

Figure 1: 3D rendering of the 5 cm^2 PEM fuel cell for in-situ WAXS/SAXS (A). Cell configured on beamline (B). Top (C), side (D) and bottom (E) view of the cell with marked cell connection details and beam directions for two possible measurement geometries. Scheme of the gas distribution system within the fuel cell (F) and detail of the flow-field (G). In-plane X-ray transmission of the PEMFC cell body, and cell body plus catalyst layer at various photon energies. (H)

large angular range allowing total scattering experiments, stopping power and detector quantum efficiency. Above this energy, Pt photoabsorption increases radiation damage and background fluorescence, while the detector efficiency decreases.

The sensitivity of PEMFCs to X-ray damage is well documented, especially the ionomer component.[39] Beam damage to fuel cell samples was evaluated in a running, hydrated cell at 10^{13} photons/s with the beam focused onto a single spot on the sample (3×20 µm^2). Slight damage to the ionomer membrane was visible by eye and the WAXS pattern was slightly reduced in intensity (less than 5%) after three hours of continuous exposure. Intermittent measurements using tenfold attenuated flux produced no detectable damage over several days, while preserving the data quality. No electrochemical signals associated with beam exposure (photocurrent) could be detected.

3.3. Electrochemical characterization

The PEMFC exhibits good performance at high gas flow rates. A 5 cm^2 cell is large enough to meaningfully evaluate electrocatalytic activity and capture the heterogeneous chemical environment present inside functional devices. Cells of this size are commonly used when evaluating novel electrocatalysts and membranes, which are typically available in very limited quantities. However, it should be emphasized that the thermal and mass transport properties of such small devices do not accurately simulate conditions inside larger systems (i.e. an automotive stack).

Traditional electrochemical experiments can be easily conducted in this setup under inert atmosphere (e.g. cyclic voltammetry, impedance spectroscopy) in addition to standard polarization measurements under air or oxygen (Figure 2). After briefly conditioning the MEA [40], high current densities can be reached. A representative hold at 1.9 A cm^{-2} (9.5 A) over two hours is shown here. The operational stability of small cells is typically limited by transient flooding phenomena [41, 42] and by the particularity of the MEA being tested. The most significant issue with the current design is the lack of active cooling. When op-

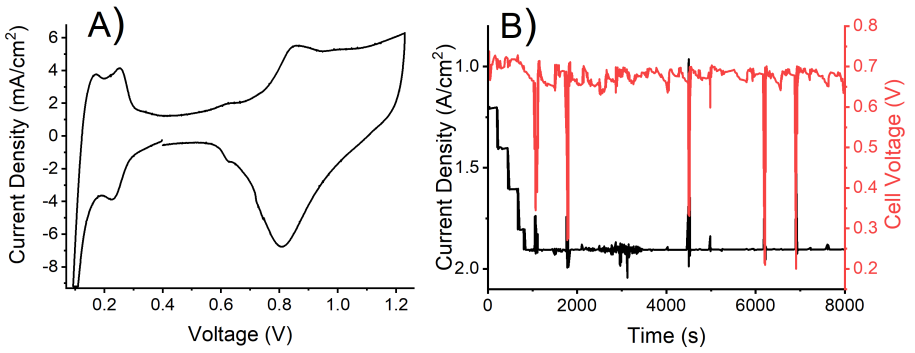

Figure 2: Electrochemical performance of the X-ray transparent cell using a commercial 5 cm^2 MEA with 0.44/0.04 $mg_{Pt}\,cm^{-2}$ catalyst coating on cathode/anode. Cyclic voltammogram under H_2/N_2 feed (A) and galvanostatic high load polarization test under H_2/O_2. 85°C, 1 bar backpressure, 50% RH, 300 sccm cathode/anode (B).

erating at or above 2 $A\,cm^{-2}$ for more than several minutes, the cell required a fan directed at the upper housing to maintain a stable temperature below 80°C.

3.4. X-ray Diffraction

A compelling feature of the grazing incidence approach using small beams is the possibility to selectively probe the membrane, anode or cathode by scanning the vertical position of the beam. The diffraction patterns from such a scan, where each material inside the MEA can be clearly differentiated, are shown in Figure 3A. These scans can be acquired relatively quickly, on the order of a few seconds and with a suitably focused beam, the cross sectional heterogeneity of the membrane and catalyst layer can be conveniently analyzed [8]. The main advantage is a greatly suppressed background from other parts of the cell, which typically complicate the analysis. Rietveld analysis of the of the diffractograms can also be performed (Figure 3B) and therefore microstructural information, such as the crystallite size, lattice parameter, and microstrain for the catalyst can be obtained for in situ/ operando experiments.

In addition, each of the diffraction patterns can be quantitatively deconvoluted into different components, further increasing the informational content of

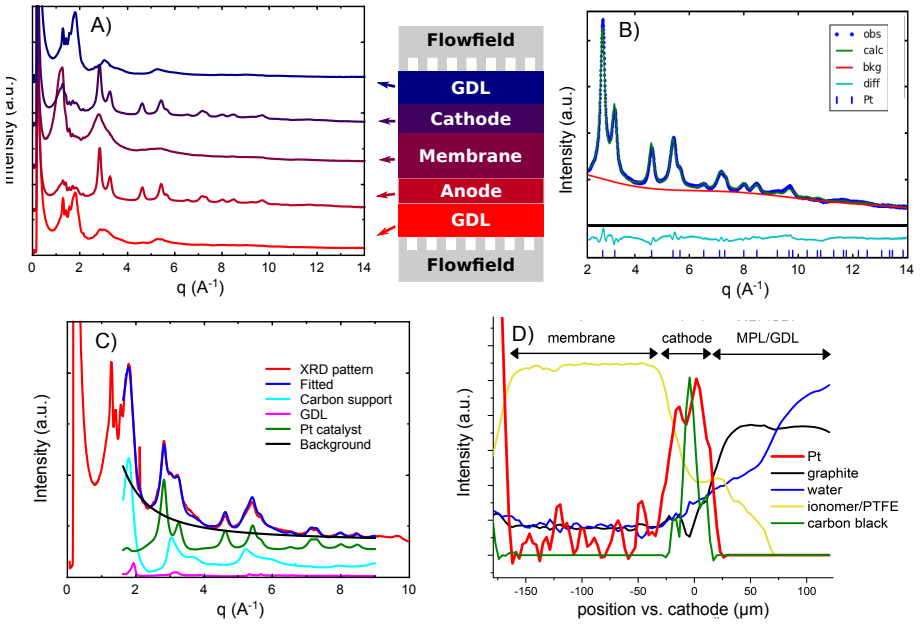

Figure 3: An example of diffraction patterns obtained from vertically scanning the position of the beam on the MEA. Each layer of the MEA can be clearly distinguished (A). The diffractograms have been vertically offset for clarity. Rietveld refinement of the Pt nanoparticles provides additional nanoscale structural information.(B) Each diffraction pattern can be further deconvoluted to its principal components allowing for quantitative analysis of each phase in the composite material (C and D).

this approach (Figure 3C). After deconvolution, the intensities of the phases can be used to map the composition of the electrode at each position during cell operation. Vertically scanning the beam through the cross section of the MEA allows for each component to be spatially distinguished (Figure 3D). Beginning at the leftmost position, the Pt from the anode is the most significant component. Then, a section approximately 125 µm thick composed of the polymer membrane is visible. Next to this, the Pt and carbon black from the catalyst layer are detected in the cathode, and then the thick GDL composed of more graphitic carbon. Water is detected through the whole cross-section, but mostly in the catalyst layer, and porous transport layers. The water signal shows a distinct increase around a position of 60 µm. This corresponds to the boundary between the microporous layer (MPL) and gas diffusion layer (GDL). Because these vertical scans can be performed in a matter of seconds, the MEA can be precisely aligned and evaluated based on the known thickness of the layers. Although the spatial resolution of the depth profiling is limited by sample alignment, the 5 cm^2 cell is sufficiently small that each layer in the MEA can be clearly resolved.

Instrumental broadening (discussed in detail in the next section) is a significant complication for large samples in high energy scattering [43]. The substantial width of the diffracting volume degrades the reciprocal space resolution at the detector. For high resolution diffraction measurements, the cell may be tilted between 0.1-0.5° to tune the effective length of the illuminated volume without the primary beam intersecting the electrode on the other side of the membrane. Alternatively, diffraction can be collected at multiple detector-sample distances, allowing for an absolute calibration of the sample position and thickness. High resolution diffraction beamlines equipped with analyzer crystals can be used to negate this effect, at the cost of measurement speed.

An MEA with a relatively thick ionomer membrane was analyzed in Figure 3 (125 µm). Cross sectional analysis of MEAs incorporating the extremely thin membranes popular for commercial automotive applications is also possible, with careful alignment. The maximum spatial resolution through the cross-

section depends on the flatness of the sample and the size of the beam. For somewhat wavy samples such as MEAs, approximately 5 µm is achievable. The diffraction from the carbon black used as a catalyst support can be differentiated from the more graphitic carbon used in the fibre paper of the gas diffusion layer (Figure 3C), allowing for detailed structural investigations of even closely related species.

3.5. Diffraction tomography

The main advantage of the presented design is the ability to perform various computed tomography (CT) measurements due to the full 360°, unobstructed field of view. Combining various advanced diffraction and imaging techniques provides structural information at variety of interesting length-scales relevant for these devices. XRD-CT probes the atomistic composition and structure [14], SAXS-CT about the mesoscale (2-50 nm) morphology [44] and μCT about the macroscale morphology, with the spatial resolution down to the size of the X-ray probe [45]. The ultimate spatial resolution of the scanning CT techniques (XRD-CT, SAXS-CT) is currently only limited by the beam size and data acquisition speed, typically on the order of minutes for one 2D slice and an hour for full 3D scans, depending on the desired number of slices. An exposure time of 133 µs per powder pattern was used.

The use of 3D tomography also relaxes the requirement for MEA samples to lie perfectly flat across the device. Multiple slices can be acquired in order to achieve higher depth resolution through the plane of the membrane versus the projected-volume, vertical scan measurements exhibited in Figure 3. The trade-offs between large samples, optical alignment, spatial resolution, and available beamtime guide the optimal data collection strategy.

The use of very hard X-rays enables the investigation of large samples and full devices, such as the PEMFC. This is due to the fact that, in contrast to softer X-rays, X-ray transmission remains significant even for thick samples (Figure 1C). However, there are currently limitations with the data analysis of X-ray diffraction/scattering computed tomography of large objects. This is due to

reconstruction artefacts related to the effect of $tan(2\theta)$ sample broadening [46]. This phenomenon is also sometimes referred to as the 'parallax effect' due to the fact that during a single point measurement, diffracted/scattered photons from different regions of the sample (along the X-ray beam path) arrive at different parts of the detector, even when diffracting at the same angle. This results in broadening of the diffraction peaks and, in extreme cases, even peak splitting (e.g. a highly crystalline phase diffracting only near the front and back of the sample). The information regarding the diffraction peak position and peak shape is therefore altered and the data must be treated with care.

New strategies for interpreting diffraction tomography data of large samples are urgently required to reduce these artefacts. All conventional tomographic algorithms (including simple filtered-back-projection to state-of-the-art iterative or bayesian-based reconstruction algorithms) cannot handle data where the parallax effect is present. Advanced reconstruction techniques to correct for these geometric aberrations at the software (i.e. new algorithms) and hardware (e.g. GPU vs CPU implementation of code) levels are currently being pursued. However, it should be emphasised that phase distribution maps can still be created using conventional tomographic algorithms, and these X-ray diffraction/scattering tomographic techniques allow one to pinpoint the location of different chemical species even in large samples and devices.

For example, in Figure 4, one XRD-CT slice measured through the cell's graphite cathode flowfield is displayed. Each voxel in the reconstructed image corresponds to one diffraction pattern which can be further analysed. In the given example, each pattern is characteristic to different materials composing the cell (C), which allows determination of the spatial distribution with very high sensitivity (A). This diffraction contrast is advantageous in comparison with conventional μCT where the electron density contrast of the composing materials is often insufficient to unambiguously resolve each component. If the components are distributed inhomogeneously as in the present case, then the signal from the cell walls (PEEK) can be separated from the signal of the material/component-of-interest (flowfield). This is demonstrated in plot (D)

where the background from the cell walls at low q is practically zero in the reconstructed diffraction patterns. The examples of reconstruction artefacts are in plots (E) (J). There the XRD patterns from a linescan across the flowfield (E) are shown for both reconstructed and raw patterns. The raw patterns correspond to the experimental data acquired during the horizontal translation of the cell during the XRD-CT scan (i.e. "projection" data). In this reconstruction, no correction for differential absorption of X-rays was made. The omission of absorption correction leads to an artefact, observed as a slight depression of the (002) peak integrated intensity in the middle of the cell (H). The parallax effect results in the splitting of the (002) peak in the reconstructed patterns (I) while only the general broadening is observed in directly measured patterns (F). Interestingly, the parallax artefact appears even in the channel areas (J) where the reconstructed graphite signal is expected to be zero. This is due to the graphite rim around the flowfield. Differences between the reconstructed and measured peak profile in the land area (G) indicates that Rietveld analysis of reconstructed patterns is difficult for large samples and should be treated with care as the peak profile is severely affected by the parallax effect (multiple or highly asymmetrical peaks).

4. Conclusions

Cell designs for in situ analysis of PEM fuel cell MEAs with high energy WAXS and SAXS are described. This cell accurately reproduced the electrochemistry of conventional devices, while allowing for facile and precise in situ X-ray analysis. The use of crudely modified commercial fuel cell equipment is no longer necessary and high quality, purpose-built sample environments are now available directly from fuel cell hardware manufacturers. As beamtime at synchrotron facilities is limited, particular attention has been given towards making the design robust, leak-free and as easy to clean and align as possible. Cells that simplify in situ measurements without compromising state-of-the-art performance will be critical for solving the longstanding issue of material degra-

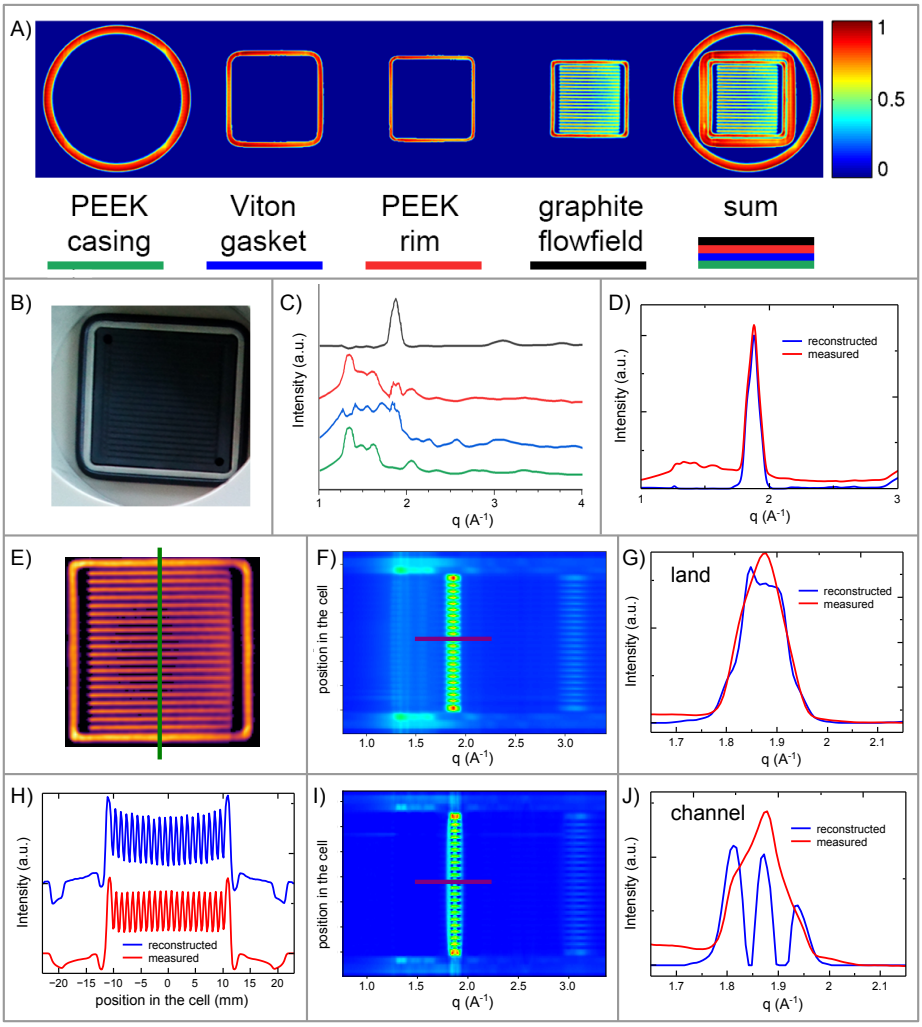

Figure 4: Assembled PEM cell imaged using XRD tomography, showing a horizontal slice through the upper flow field plate. The component distribution maps made from XRD signals characteristic for different fuel cell materials are shown in panel (A). The color indicates the intensity of the fitted phase at that location. The photograph of the flowfield for comparison is presented in panel (B). The mean diffraction patterns from the four regions shown in image (A) are presented in panel (C). A comparison between reconstructed and raw diffraction patterns signals is presented in panel (D). A detailed reconstructed map of the graphite flowfield with a marked linescan used in panels (F-J) are shown in panel (E). The integrated intensity of the graphite (002) peak along the linescan for the reconstructed and raw XRD patterns is presented in panel (H). XRD patterns along the linescan for reconstructed and raw diffraction data are shown in panels (I) and (F) respectively. Each row corresponds to the XRD pattern at a certain position along the linescan (i.e. 230 patterns in total). A comparison between the graphite (002) profiles of the reconstructed and raw patterns on land and channel areas is provided in panels (G) and (J) respectively.

dation in fuel cell devices. Detailed studies to investigate the structural changes of electrocatalyst samples under operando conditions are presently underway.

Acknowledgement

This work was financially supported by an NSERC (Canada) Discovery grant and by the CaRPE-FC network. IM acknowledges NSERC CGSD and MSFSS scholarship funding. AV is supported (in part) through funding received from the European Union Horizon 2020 research and innovation programme under Grant Agreement No. 679933 (MEMERE project). All authors thank ESRF ID31 beamline staff for expert technical support.

References

[1] C. G. Schroer, I. Agapov, W. Brefeld, R. Brinkmann, Y.-C. Chae, H.-C. Chao, M. Eriksson, J. Keil, X. Nuel Gavaldà, R. Röhlsberger, O. H. Seeck, M. Sprung, M. Tischer, R. Wanzenberg, E. Weckert, IUCr, PETRA IV: the ultralow-emittance source project at DESY, Journal of Synchrotron Radiation 25 (5) (2018) 1277–1290. doi:10.1107/S1600577518008858.
URL http://scripts.iucr.org/cgi-bin/paper?S1600577518008858

[2] P. Raimondi, ESRF-EBS: The Extremely Brilliant Source Project, Synchrotron Radiation News 29 (6) (2016) 8–15. doi:10.1080/08940886.2016.1244462.
URL https://www.tandfonline.com/doi/full/10.1080/08940886.2016.1244462

[3] V. Honkimäki, Engineering Materials Research at ESRF, Synchrotron Radiation News 30 (3) (2017) 48–54. doi:10.1080/08940886.2017.1316132.
URL https://www.tandfonline.com/doi/full/10.1080/08940886.2017.1316132

[4] U. Hejral, P. Müller, M. Shipilin, J. Gustafson, D. Franz, R. Shayduk, U. Rütt, C. Zhang, L. R. Merte, E. Lundgren, V. Vonk, A. Stierle, High-energy x-ray diffraction from surfaces and nanoparticles, Physical Review B 96 (19) (2017) 195433. doi:10.1103/PhysRevB.96.195433.
URL https://link.aps.org/doi/10.1103/PhysRevB.96.195433

[5] D. L. Bish, S. A. Howard, Quantitative phase analysis using the Rietveld method, Journal of Applied Crystallography 21 (2) (1988) 86–91. doi:10.1107/S0021889887009415.
URL http://scripts.iucr.org/cgi-bin/paper?S0021889887009415

[6] S. Huotari, T. Pylkkänen, R. Verbeni, G. Monaco, K. Hämäläinen, Direct tomography with chemical-bond contrast, Nature Materials 10 (7) (2011) 489–493. doi:10.1038/nmat3031.
URL http://www.nature.com/articles/nmat3031

[7] H. L. Xin, J. A. Mundy, Z. Liu, R. Cabezas, R. Hovden, L. F. Kourkoutis, J. Zhang, N. P. Subramanian, R. Makharia, F. T. Wagner, D. A. Muller, Atomic-Resolution Spectroscopic Imaging of Ensembles of Nanocatalyst Particles Across the Life of a Fuel Cell, Nano Letters 12 (1) (2012) 490–497. doi:10.1021/nl203975u.
URL http://pubs.acs.org/doi/10.1021/nl203975u

[8] A. Kneer, J. Jankovic, D. Susac, A. Putz, N. Wagner, M. Sabharwal, M. Secanell, Correlation of Changes in Electrochemical and Structural Parameters due to Voltage Cycling Induced Degradation in PEM Fuel Cells, Journal of The Electrochemical Society 165 (6) (2018) F3241–F3250. doi:10.1149/2.0271806jes.
URL http://jes.ecsdl.org/lookup/doi/10.1149/2.0271806jes

[9] Y. Cai, J. M. Ziegelbauer, A. M. Baker, W. Gu, R. S. Kukreja, A. Kongkanand, M. F. Mathias, R. Mukundan, R. L. Borup, Electrode edge cobalt cation migration in an operating fuel cell: An in situ micro-x-ray fluorescence study, Journal of The Electrochemical Society

165 (6) (2018) F3132–F3138. arXiv:http://jes.ecsdl.org/content/165/6/F3132.full.pdf+html, doi:10.1149/2.0201806jes.
URL http://jes.ecsdl.org/content/165/6/F3132.abstract

[10] G. Harding, J. Kosanetzky, U. Neitzel, X-ray diffraction computed tomography, Medical Physics 14 (4) (1987) 515–525. doi:10.1118/1.596063.
URL http://doi.wiley.com/10.1118/1.596063

[11] U. Kleuker, P. Suortti, W. Weyrich, P. Spanne, Feasibility study of x-ray diffraction computed tomography for medical imaging, Physics in Medicine and Biology 43 (10) (1998) 2911–2923. doi:10.1088/0031-9155/43/10/017.
URL http://stacks.iop.org/0031-9155/43/i=10/a=017?key=crossref.b60029ca1f3c29cd2dc49b3b6bcef8db

[12] P. Bleuet, E. Welcomme, E. Dooryhée, J. Susini, J.-L. Hodeau, P. Walter, Probing the structure of heterogeneous diluted materials by diffraction tomography, Nature Materials 7 (6) (2008) 468–472. doi:10.1038/nmat2168.
URL http://www.nature.com/articles/nmat2168

[13] S. D. M. Jacques, M. Di Michiel, S. A. J. Kimber, X. Yang, R. J. Cernik, A. M. Beale, S. J. L. Billinge, Pair distribution function computed tomography, Nature Communications 4 (1) (2013) 2536. doi:10.1038/ncomms3536.
URL http://www.nature.com/articles/ncomms3536

[14] A. Vamvakeros, S. D. Jacques, M. Di Michiel, D. Matras, V. Middelkoop, I. Z. Ismagilov, E. V. Matus, V. V. Kuznetsov, J. Drnec, P. Senecal, A. M. Beale, 5D operando tomographic diffraction imaging of a catalyst bed, Nature communications 9 (1) (2018) 4751. doi:10.1038/s41467-018-07046-8.
URL http://www.nature.com/articles/s41467-018-07046-8

[15] D. Finegan, A. Vamvakeros, L. Cao, C. Tan, T. Heenan, S. Daemi, S. Jacques, A. M. Beale, M. Di Michiel, K. Smith, D. J. Brett, P. R. Shearing, C. Ban, Spatially resolving lithiation in si-graphite composite electrodes via in situ high-energy xrd-ct, Nano Lettersdoi:10.1021/acs.nanolett.9b00955.

[16] T. Li, T. M. M. Heenan, M. F. Rabuni, B. Wang, N. M. Farandos, G. H. Kelsall, D. Matras, C. Tan, X. Lu, S. D. M. Jacques, D. J. L. Brett, P. R. Shearing, M. Di Michiel, A. M. Beale, A. Vamvakeros, K. Li, Design of next-generation ceramic fuel cells and real-time characterization with synchrotron X-ray diffraction computed tomography, Nature Communications 10 (1) (2019) 1497. doi:10.1038/s41467-019-09427-z.
URL http://www.nature.com/articles/s41467-019-09427-z

[17] R. Kuhn, J. Scholta, P. Krüger, C. Hartnig, W. Lehnert, T. Arlt, I. Manke, Measuring device for synchrotron X-ray imaging and first results of high temperature polymer electrolyte membrane fuel cells, Journal of Power Sources 196 (12) (2011) 5231–5239. doi:10.1016/j.jpowsour.2010.11.025.
URL https://www.sciencedirect.com/science/article/abs/pii/S0378775310019312

[18] L. Dubau, L. Castanheira, G. Berthom, F. Maillard, An identical-location transmission electron microscopy study on the degradation of pt/c nanoparticles under oxidizing, reducing and neutral atmosphere, Electrochimica Acta 110 (2013) 273 – 281, eLECTROCHEMISTRY FOR ADVANCED MATERIALS, TECHNOLOGIES AND INSTRUMENTATION. doi:https://doi.org/10.1016/j.electacta.2013.03.184.
URL http://www.sciencedirect.com/science/article/pii/S0013468613006233

[19] E. Leonard, A. D. Shum, S. Normile, D. C. Sabarirajan, D. G. Yared, X. Xiao, I. V. Zenyuk, Operando x-ray tomography and sub-second ra-

diography for characterizing transport in polymer electrolyte membrane electrolyzer, Electrochimica Acta 276. doi:10.1016/j.electacta.2018.04.144.

[20] S. J. Normile, D. C. Sabarirajan, O. Calzada, V. D. Andrade, X. Xiao, P. Mandal, D. Y. Parkinson, A. Serov, P. Atanassov, I. V. Zenyuk, Direct observations of liquid water formation at nano- and micro-scale in platinum group metal-free electrodes by operando x-ray computed tomography, Materials Today Energy 9 (2018) 187 – 197. doi:https://doi.org/10.1016/j.mtener.2018.05.011.
URL http://www.sciencedirect.com/science/article/pii/S2468606917303350

[21] J. A. Gilbert, A. J. Kropf, N. N. Kariuki, S. DeCrane, X. Wang, S. Rasouli, K. Yu, P. J. Ferreira, D. Morgan, D. J. Myers, In-operando anomalous small-angle x-ray scattering investigation of pt3co catalyst degradation in aqueous and fuel cell environments, Journal of The Electrochemical Society 162 (14) (2015) F1487–F1497. arXiv:http://jes.ecsdl.org/content/162/14/F1487.full.pdf+html, doi:10.1149/2.0531514jes.
URL http://jes.ecsdl.org/content/162/14/F1487.abstract

[22] E. L. Redmond, B. P. Setzler, P. Juhas, S. J. L. Billinge, T. F. Fuller, In-Situ Monitoring of Particle Growth at PEMFC Cathode under Accelerated Cycling Conditions, Electrochemical and Solid-State Letters 15 (5) (2012) B72. doi:10.1149/2.004206esl.
URL http://esl.ecsdl.org/cgi/doi/10.1149/2.004206esl

[23] O. Sekizawa, T. Uruga, K. Higashi, T. Kaneko, Y. Yoshida, T. Sakata, Y. Iwasawa, Simultaneous Operando Time-Resolved XAFS-XRD Measurements of a Pt/C Cathode Catalyst in Polymer Electrolyte Fuel Cell under Transient Potential Operations, ACS Sustainable Chemistry and Engineering 5 (5) (2017) 3631–3636. doi:10.1021/acssuschemeng.7b00052.

[24] T. Asset, C. J. Gommes, J. Drnec, P. Bordet, R. Chattot, I. Martens,

J. Nelayah, N. Job, F. Maillard, L. Dubau, Disentangling the Degradation Pathways of Highly Defective PtNi/C Nanostructures An Operando Wide and Small Angle X-Ray Scattering Study, ACS Catalysisdoi:10.1021/acscatal.8b02665.
URL http://pubs.acs.org/doi/10.1021/acscatal.8b02665

[25] N. Ishiguro, T. Saida, T. Uruga, O. Sekizawa, K. Nagasawa, K. Nitta, T. Yamamoto, S. Ohkoshi, T. Yokoyama, M. Tada, Structural kinetics of a Pt/C cathode catalyst with practical catalyst loading in an MEA for PEFC operating conditions studied by in situ time-resolved XAFS, Physical Chemistry Chemical Physics 15 (43) (2013) 18827–18834. doi:10.1039/c3cp52578c.
URL http://xlink.rsc.org/?DOI=c3cp52578c

[26] S. S. Kocha, K. Shinozaki, J. W. Zack, D. J. Myers, N. N. Kariuki, T. Nowicki, V. Stamenkovic, Y. Kang, D. Li, D. Papageorgopoulos, Best Practices and Testing Protocols for Benchmarking ORR Activities of Fuel Cell Electrocatalysts Using Rotating Disk Electrode, Electrocatalysis 8 (4) (2017) 366–374. doi:10.1007/s12678-017-0378-6.

[27] K. Shinozaki, B. S. Pivovara, S. S. Kocha, Enhanced Oxygen Reduction Activity on Pt/C for Nafion-free, Thin, Uniform Films in Rotating Disk Electrode Studies, ECS Transactions 58 (1) (2013) 15–26. doi:10.1149/05801.0015ecst.

[28] K. Shinozaki, J. W. Zack, R. M. Richards, B. S. Pivovar, S. S. Kocha, Oxygen Reduction Reaction Measurements on Platinum Electrocatalysts Utilizing Rotating Disk Electrode Technique, Journal of The Electrochemical Society 162 (10) (2015) F1144–F1158. doi:10.1149/2.1071509jes.
URL http://jes.ecsdl.org/lookup/doi/10.1149/2.1071509jes

[29] R. D. Smith, C. Pasquini, S. Loos, P. Chernev, K. Klingan, P. Kubella, M. R. Mohammadi, D. González-Flores, H. Dau, Geometric distortions

in nickel (oxy)hydroxide electrocatalysts by redox inactive iron ions, Energy and Environmental Science 11 (9) (2018) 2476–2485. doi:10.1039/c8ee01063c.

[30] S. Y. Lai, D. Ding, M. Liu, M. Liu, F. M. Alamgir, Operando and in situ X-ray spectroscopies of degradation in LaSrCoFeO thin film cathodes in fuel cells, ChemSusChem 7 (11) (2014) 3078–3087. doi:10.1002/cssc.201402670.

[31] Z. Nagy, H. You, Applications of surface X-ray scattering to electrochemistry problems, Electrochimica Acta 47 (19) (2002) 3037–3055. doi:10.1016/S0013-4686(02)00223-2.

[32] P. J. Ferreira, G. J. la O', Y. Shao-Horn, D. Morgan, R. Makharia, S. Kocha, H. A. Gasteiger, Instability of PtC Electrocatalysts in Proton Exchange Membrane Fuel Cells, Journal of The Electrochemical Society 152 (11) (2005) A2256. doi:10.1149/1.2050347.
URL http://jes.ecsdl.org/cgi/doi/10.1149/1.2050347

[33] G. Ashiotis, A. Deschildre, Z. Nawaz, J. P. Wright, D. Karkoulis, F. E. Picca, J. Kieffer, The fast azimuthal integration Python library: PyFAI, Journal of Applied Crystallography 48 (2) (2015) 510–519. doi:10.1107/S1600576715004306.
URL http://scripts.iucr.org/cgi-bin/paper?S1600576715004306

[34] A. Vamvakeros, S. D. Jacques, V. Middelkoop, M. Di Michiel, C. K. Egan, I. Z. Ismagilov, G. B. Vaughan, F. Gallucci, M. Van Sint Annaland, P. R. Shearing, R. J. Cernik, A. M. Beale, Real time chemical imaging of a working catalytic membrane reactor during oxidative coupling of methane, Chemical Communications 51 (64) (2015) 12752–12755. doi:10.1039/c5cc03208c.
URL http://dx.doi.org/10.1039/C5CC03208C

[35] N. Ishiguro, T. Saida, T. Uruga, S.-i. Nagamatsu, O. Sekizawa, K. Nitta, T. Yamamoto, S.-i. Ohkoshi, Y. Iwasawa, T. Yokoyama, M. Tada,

Operando Time-Resolved X-ray Absorption Fine Structure Study for Surface Events on a Pt3Co/C Cathode Catalyst in a Polymer Electrolyte Fuel Cell during Voltage-Operating Processes, ACS Catalysis 2 (7) (2012) 1319–1330. doi:10.1021/cs300228p.
URL http://pubs.acs.org/doi/10.1021/cs300228p

[36] H. Imai, K. Izumi, M. Matsumoto, Y. Kubo, K. Kato, Y. Imai, In Situ and Real-Time Monitoring of Oxide Growth in a Few Monolayers at Surfaces of Platinum Nanoparticles in Aqueous Media, Journal of the American Chemical Society 131 (7) (2009) 6293–6300. doi:10.1021/ja810036h.

[37] S. I. Nagamatsu, T. Arai, M. Yamamoto, T. Ohkura, H. Oyanagi, T. Ishizaka, H. Kawanami, T. Uruga, M. Tada, Y. Iwasawa, Potential-dependent restructuring and hysteresis in the structural and electronic transformations of Pt/C, Au(Core)-Pt(Shell)/C, and Pd(Core)-Pt(Shell)/C cathode catalysts in polymer electrolyte fuel cells characterized by in situ X-ray absorption fine st, Journal of Physical Chemistry C 117 (25) (2013) 13094–13107. doi:10.1021/jp402438e.

[38] M. Osterhoff, C. Eberl, J. Soltau, H.-U. Krebs, Ultra-high-aspect multilayer zone plates for even higher x-ray energies, in: C. Morawe, A. M. Khounsary, S. Goto (Eds.), Advances in X-Ray/EUV Optics and Components XII, Vol. 10386, SPIE, 2017, p. 7. doi:10.1117/12.2271139.
URL https://www.spiedigitallibrary.org/conference-proceedings-of-spie/10386/2271139/Ultra-high-aspect-multilayer-zone-plates-for-even-higher-x/10.1117/12.2271139.full

[39] I. Martens, L. G. A. Melo, D. P. Wilkinson, D. Bizzotto, A. P. Hitchcock, Characterization of x-ray damage to perfluorosulfonic acid using correlative microscopy, The Journal of Physical Chemistry C 0 (ja) (0) null. arXiv:https://doi.org/10.1021/acs.jpcc.9b03924, doi:10.

1021/acs.jpcc.9b03924.
URL https://doi.org/10.1021/acs.jpcc.9b03924

[40] M. Blanco, Study of Selected Water Management Strategies for Proton Exchange Membrane Fuel Cells, Ph.D. thesis, University of British Columbia (2011).

[41] S. Litster, C. R. Buie, T. Fabian, J. K. Eaton, J. G. Santiago, Active Water Management for PEM Fuel Cells, Journal of The Electrochemical Society 154 (10) (2007) B1049. doi:10.1149/1.2766650.
URL http://jes.ecsdl.org/cgi/doi/10.1149/1.2766650

[42] H. Li, Y. Tang, Z. Wang, Z. Shi, S. Wu, D. Song, J. Zhang, K. Fatih, J. Zhang, H. Wang, Z. Liu, R. Abouatallah, A. Mazza, A review of water flooding issues in the proton exchange membrane fuel cell (mar 2008). doi:10.1016/j.jpowsour.2007.12.068.
URL https://www.sciencedirect.com/science/article/abs/pii/S0378775307027991

[43] X. Qiu, E. S. Božin, P. Juhas, T. Proffen, S. J. Billinge, Reciprocal-space instrumental effects on the real-space neutron atomic pair distribution function, Journal of Applied Crystallography 37 (1) (2004) 110–116. doi:10.1107/S0021889803026670.
URL http://scripts.iucr.org/cgi-bin/paper?S0021889803026670

[44] M. Choi, B. Ghammraoui, A. Badano, Small-angle X-ray scattering characteristics of mouse brain: Planar imaging measurements and tomographic imaging simulations, PLoS ONE 12 (10) (2017) e0186451. doi:10.1371/journal.pone.0186451.
URL https://dx.plos.org/10.1371/journal.pone.0186451

[45] P. Chaurand, W. Liu, D. Borschneck, C. Levard, M. Auffan, E. Paul, B. Collin, I. Kieffer, S. Lanone, J. Rose, J. Perrin, Multi-scale X-ray computed tomography to detect and localize metal-based nanomaterials

in lung tissues of in vivo exposed mice, Scientific Reports 8 (1) (2018) 4408. doi:10.1038/s41598-018-21862-4.
URL http://www.nature.com/articles/s41598-018-21862-4

[46] A. M. Beale, S. D. Jacques, E. K. Gibson, M. D. Michiel, Progress towards five dimensional diffraction imaging of functional materials under process conditions, Coordination Chemistry Reviews 277-278 (2014) 208 – 223, following Chemical Structures using Synchrotron Radiation. doi:https://doi.org/10.1016/j.ccr.2014.05.008.
URL http://www.sciencedirect.com/science/article/pii/S001085451400143X